



Impact of co-doping with Mn and Co/Mn on the structural, microstructural, dielectric, impedance, and magnetic characteristics of multiferroic bismuth ferrite nanoparticles

B. Dhanalakshmi¹ · G. M. Sravani² · J. Suresh³ · P. V. S. S. N. Reddy⁴ · K. Eswara Rao⁵ · Sudhakar Jyothula⁶ · Chandra Sekhar Beera⁷

Received: 27 March 2023 / Accepted: 21 May 2023 / Published online: 31 May 2023
© The Author(s), under exclusive licence to Springer-Verlag GmbH, DE part of Springer Nature 2023

Abstract

Bismuth ferrite with manganese doping ($\text{BiFe}_{0.95}\text{Mn}_{0.05}\text{O}_3$ or BFMO) and bismuth ferrite with cobalt and manganese doping ($\text{Bi}_{0.95}\text{Co}_{0.05}\text{Fe}_{0.95}\text{Mn}_{0.05}\text{O}_3$ or BCoFMO) were both synthesized as nanocrystalline powders by the sol–gel autocombustion technique. X-ray diffraction examination of the powders indicates a rhombohedral distortion in the perovskite phase in both samples. The calcined powders were examined for their microstructure and elemental composition with high resolution transmission electron microscopy (HRTEM) and energy dispersive X-ray spectroscopy (EDAX), respectively. Scanning electron microscopy (SEM) was used to examine the microstructures of sintered BMFO and BCoFMO specimens at room temperature. Dielectric characteristics were studied at various frequencies and temperatures and found to follow space charge polarization. At ambient temperature, a vibrating sample magnetometer was used to analyse the materials' magnetic behaviour (M–H loops). Saturation magnetization is significantly increased with increased coercivity in the BCoFMO sample compared to the other sample. Improved structural, dielectric, and magnetic values in these doped systems, however, suggest they'd be an excellent fit for spintronic, multifunctional memories, sensors, and actuators.

Keywords Nanoparticles · HRTEM · XRD · Dielectric measurements · M–H loops

1 Introduction

Multiferroics, which are ferromagnetic, ferroelectric, and ferroelastic in one phase, are vital for the creation of multifunctional devices [1–3]. Due to its several ferroic orders, multiferroics are fascinating. Multiple orders in a phase make these materials more versatile for usage in different contexts. The coupling between ferroic orders is highly influenced by the origin of its occurrence (for example, the availability of partially filled “d” electrons for magnetism and the existence of vacant “d” shells for ferroelectricity) as well as other structural characteristics. Transition metals with “d” electrons reduce off-centre ferroelectric distortion in several situations [4–6]. Controlling other ferroic features is crucial to developing unique magnetoelectric properties and designing novel multifunctional devices such multistate memory, spin rotation-based devices in spintronic applications, highly sensitive electric and magnetic sensors, etc. [4, 7–9]. This phenomenon is needed to develop unique magnetoelectric characteristics and design novel multifunctional devices. Single-phase and multi-phase multiferroics are the primary kinds of constituent phases

✉ B. Dhanalakshmi
deepthi0527@gmail.com

¹ Department of Physics, Vignan's Institute of Information Technology (VIIT-A), Visakhapatnam, Andhra Pradesh 530049, India

² Department of Physics, Andhra University, Visakhapatnam 530003, India

³ Department of Physics, BVC College of Engineering, Rajamahendravaram 533102, India

⁴ Department of Physics, Government College (A), Rajamahendravaram 533102, India

⁵ Department of Chemistry, Sasi Institute of Technology and Engineering (A), Tadepalligudem 534101, India

⁶ Department of Electronics and Communication Engineering, Vignan's Institute of Engineering for Women, Visakhapatnam 530046, India

⁷ Department of Physics, Vignan's Institute of Engineering for Women, Visakhapatnam 530046, India

used in multiferroic design and manufacturing [1, 2]. These two main processes are involved in multiferroic design and manufacture. BiFeO_3 , YMnO_3 , TbMnO_3 , HoMnO_3 , $\text{Ni}_3\text{V}_2\text{O}_8$, and TbMn_2O_5 are among the many single-phase multiferroics identified. These materials have weak magneto-electric (ME) coupling constants because their coupling origins are significantly varied [10]. Researchers used several methods to improve coupling in these systems. These strategies included chemical modifications like doping with foreign elements by selecting probable site preferences (like A or B sites in ABO_3 or AB_2O_4 structures) of the sample or adding a strong second phase of ferromagnetic, ferroelectric, and ferroelastic phase to the single phase to meet requirements and improve structural modifications. Due of its unique multiferroic characteristics, bismuth ferrite (BiFeO_3 or BFO) with an ABO_3 perovskite structure is the current research trend. The ferroelectric Curie temperature is 830°C , and the ferromagnetic Neel's temperature is 370°C . G-type antiferromagnetic spin construction and the superimposed incommensurate cycloid spin structure with a periodicity of 620 \AA nullify this sample's magnetism. Before any other chemical alterations may be successful, the sample must be changed from antiferromagnetic to probably ferro/ferrite by compensating its cycloid symmetry in bismuth ferrite. BFO's magnetoelectric coupling needs to be improved despite multiple attempts to improve its multiferroic properties by exchanging divalent and trivalent ions at the Bi and Fe sites [10–13]. In order to address this problem, the current work intends to change the crystal structure of BFO by including cobalt (Co) and manganese (Mn) ions in the A-site and B-site for one sample, and manganese (Mn) ions in the B-site and A-site for the other sample, respectively. The investigation of the effects of single and co-doping on these samples may now reveal the typical mechanism responsible for boosting or changing the bismuth ferrite lattice's structural, microstructural, dielectric, and magnetic characteristics. Additionally, the sol–gel autocombustion method is preferred in the current work for the synthesis of initial powder samples at nano scales because the properties of multiferroics at these scales are frequently superior to those of their bulk counterparts due to improved structural uniformity and homogeneity [11, 14]. So, utilizing the sol–gel autocombustion approach, single phase Mn doped BFO and Mn and Co co-doped BFO multiferroics were synthesized, and in the present study it is examined how the doping effect affects structural, microstructural, dielectric, impedance, and magnetic characteristics.

2 Experimental

Wet chemical sol–gel autocombustion is recognized as the simplest, quickest, and least expensive process for producing fully crystalline, homogeneous nanoparticles in a single reaction under ambient experimental conditions [15]. The

analytical reagents of bismuth nitrate [$\text{Bi}(\text{NO}_3)_3 \cdot 5\text{H}_2\text{O}$], cobalt nitrate [$\text{Co}(\text{NO}_3)_2 \cdot 6\text{H}_2\text{O}$], ferric nitrate [$\text{Fe}(\text{NO}_3)_3 \cdot 9\text{H}_2\text{O}$], manganese nitrate [$\text{Mn}(\text{NO}_3)_2 \cdot 4\text{H}_2\text{O}$], and citric acid were used to synthesise Mn and Co & Mn co-doped BFO nanoparticles with the chemical formula $\text{BiFe}_{0.95}\text{Mn}_{0.05}\text{O}_3$ and $\text{Bi}_{0.95}\text{Co}_{0.05}\text{Fe}_{0.95}\text{Mn}_{0.05}\text{O}_3$. First, aqueous solutions of all compounds were prepared separately by dissolving the metal nitrates in minimal amounts of distilled water and bismuth nitrate in minimal amounts of nitric acid. Then, according to the chemical formulas, all aqueous solutions were combined while maintaining a 1:1 ratio of all metal nitrates to citric acid. Ammonia (NH_3) was utilized to bring the pH level of the solution to 7 in order to neutralize it. These solutions were now heated at $80\text{--}90^\circ\text{C}$ for 2 h while being constantly stirred to form dry gel. At this point, the temperature of the dried gel was raised to $100\text{--}130^\circ\text{C}$ in order to initiate ignition at any given time. The gels appear at the ignition temperature. Following this stage, self-propagating combustion occurs with quick and vigorous flames until the gels are totally changed into ash-like flakes. Using a spatula, these flakes were gently compressed to produce fine nano powders. To promote crystallisation and remove any remaining impurities, the nanoparticles were calcined at 600°C for 2 h at heating and cooling rates of $5^\circ\text{C}/\text{min}$. The pressed compacts were finally sintered at 800°C for 4 h with heating and cooling rates of $5^\circ\text{C}/\text{min}$. The synthesized nanopowders and sintered pellets of the specimens have subsequently undergone different characterizations. X-ray diffraction (XRD) analyses were performed on the specimens using an XPERT-PRO X-ray powder diffractometer with $\text{Cu K}\alpha$ radiation, $\lambda = 1.5406\text{ \AA}$, within the 2θ range of $20^\circ\text{--}80^\circ$ for phase confirmation. Fourier transform infrared (FTIR) spectra were collected using a Perkin Elmer-6100 FTIR instrument. High-resolution transmission electron microscopy (HRTEM: Model—JEOL JEM 2100) and scanning electron microscopy (SEM: Model—Hitachi S-3400N) techniques were used to quantify the particle and grain sizes of the calcined nanopowders and sintered pellets, respectively. Additionally, elemental analysis was performed through the implementation of energy dispersive X-ray spectroscopy (EDAX) technique. Dielectric studies were made on the samples using an Agilent LCR meter in the frequency range from 1 Hz to 10 MHz and also at different temperatures in the range from 30 to 300°C . Magnetic hysteresis loops were also performed on the samples with a SQUID VSM 3474-140 GMW magnetometer to evaluate their magnetic character.

3 Results and discussion

3.1 XRD analysis

Figures 1a and b display the X-ray diffraction (XRD) patterns of the manganese doped ($\text{BiFe}_{0.95}\text{Mn}_{0.05}\text{O}_3$) or

BFMO) and cobalt and manganese co-doped ($\text{Bi}_{0.95}\text{Co}_{0.05}\text{Fe}_{0.95}\text{Mn}_{0.05}\text{O}_3$ or BCoFMO) bismuth ferrite multiferroic samples. All peaks in Fig. 1a and b correspond to the BFMO and BCoFMO phases in the rhombohedrally deformed perovskite structure of space group R3c (JCPDS 72-2035). The principal peaks of both samples were well matched, while the remainder of the peak intensities had nearly identical magnitudes. On the basis of the acquired XRD peaks, mullite ($\text{Bi}_2\text{Fe}_4\text{O}_9$) and sillenite ($\text{Bi}_{36}\text{Fe}_2\text{O}_{57}$) were identified as impurities in both of the samples. These unavoidable extra phases in bismuth ferrite are the result of the normal kinetics of its development during the synthesis process, as described in numerous researches [11, 16–19]. In addition, it was determined that these impurity phases exhibit typical antiferromagnetic behaviour and so contribute negligibly to the magnetic order in the present system of samples.

The mean crystallite sizes (DP) of the produced particles were calculated using the XRD patterns and the Scherrer equation, $D = 0.9\lambda/\beta\cos\theta$, where ' λ ' is the wavelength of the X-rays employed, i.e., 0.15406 nm, ' β ' is the full-width at half maximum (FWHM), and ' θ ' is the Bragg angle. As depicted in the inset of Fig. 1, full width at half maximum (β) values were determined using Gaussian fit best fit. Despite bismuth ferrite's orientation in a deformed rhombohedral perovskite structure, its unit cell has hexagonal

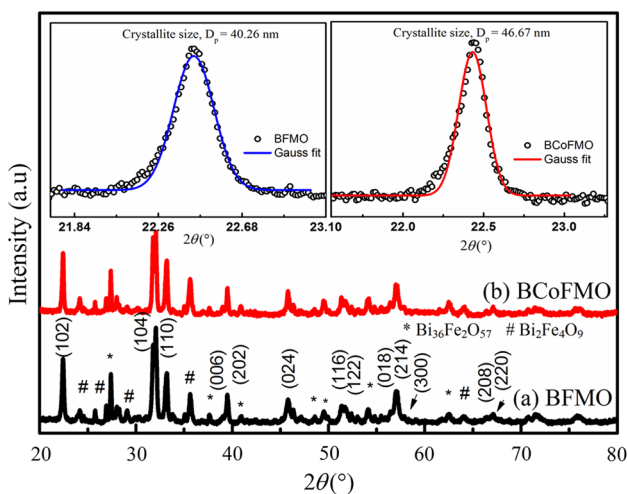


Fig. 1 XRD patterns of **a** BFMO and **b** BCoFMO multiferroic samples. Gaussian fit for both samples shown in inset

symmetry. All particle sizes, lattice parameters, and cell volumes were computed using the Scherrer equation and hexagonal crystallographic equations, respectively, and are displayed in Table 1 along with magnetic parameters to be examined in the following section. The difference in crystallite sizes and lattice characteristics between the two samples was related to the difference in ionic radius of the doping elements.

Since the ionic radii of the parent sites of Bi and Fe in sixfold coordination are 1.03 Å and 0.645 Å, those of Co and Mn in sixfold coordination and eightfold coordination are 0.545 Å and 0.645 Å, respectively [20]. According to the chemical formulas, it is evident from the values of these ionic radii that doping elements with lesser and equal magnitudes can easily enter and settle in the correct lattice sites. The increased crystallite size and modest differences in lattice characteristics found in BCoFMO relative to BFMO can be explained by the presence of extra ions (cobalt) and their respective cationic and anionic site preferences. Clearly, this could result in the stretching of the lattice and, consequently, the associated lattice parameters. In addition to site preferences, forced migrations of ions between distinct lattice sites may potentially contribute to cell volume fluctuation [11]. The obtained results in the present samples were consistent with the aforementioned explanations.

3.1.1 FTIR analysis

Fourier transform infrared spectroscopy (FTIR) is a useful method for obtaining qualitative structural information on functional groups and their links in multiferroics. The atomic mass, cationic radius, cation–anion bond lengths, etc. are said to affect the spectra's absorption bands [18, 19]. In order to comprehend the formation of fundamental absorption bands in BFMO and BCoFMO samples, FTIR spectra were collected in the wavenumber range 400–1000 cm^{-1} and are depicted in Fig. 2. Strong absorption bands between 450 and 550 cm^{-1} confirm the perovskite formation in both samples. The bending vibration of the Fe–O bond in the FeO_6 octahedral unit and the BiO_6 octahedral structure unit are responsible for these absorption peaks. The spectrum of BCoFMO reveals a small frequency shift in the peak near 500 cm^{-1} compared to the corresponding peak of BFMO, as well as the presence of an extra shoulder peak near 768 cm^{-1} . Due to

Table 1 Structural and magnetic parameters of $\text{BiFe}_{0.95}\text{Mn}_{0.05}\text{O}_3$ and $\text{Bi}_{0.95}\text{Co}_{0.05}\text{Fe}_{0.95}\text{Mn}_{0.05}\text{O}_3$ multiferroic samples

Sample	Lattice parameters		Cell volume (Å^3)	Crystallite size, D_p (nm) ± 0.50	Magnetic saturation, M_s (emu/g)	Coercivity, H_c (Oe)	Retentivity, M_r (emu/g)
	$a = b$ (Å)	c (Å)					
BFMO	5.5788	13.8642	375.3952	40.61	1.7345	187.6548	0.3133
BCoFMO	5.5797	13.8485	375.0991	46.42	5.1204	1500.0496	2.4717

the introduction of doped ions into the Bi–O and Fe–O lattices, the observed peak displacement and additional peak formation in both samples may result from a corresponding change in the bond lengths of Bi–O and Fe–O [18].

3.2 Microstructural studies

3.2.1 High resolution transmission electron microscopy (HRTEM) studies

The characteristics of multiferroic ceramics are highly dependent on the microstructural modification and chemical purity of the doped sample. Therefore, calcined nanopowders of multiferroics were examined for their microstructural features at room temperature using high resolution transmission electron microscopy (HRTEM) in order to comprehend their effect on various attributes. Figure 3 displays the obtained HRTEM images of the BFMO and BCoFMO samples. Using imageJ software [21], the average particle sizes of two samples are determined to be between 40 and 48 nm for the BFMO and 45 and 56 nm for the BCoFMO.

In addition, energy dispersive X-ray spectra (EDAX) were collected to evaluate the chemical purity of the materials. It is crucial to obtain the sample's purest form for which it was produced. Figure 4 depicts a typical BCoFMO spectrum sample (c). The patterns clearly demonstrate the presence of only the elements that make up the BCoFMO single-phase multiferroic. Since the experiment was conducted on a copper (Cu) grid, the spectrum reflected the same peaks in addition to the primary peaks

of Bi, Co, Fe, and Mn. Thus, it is evident that the sample has no extra phases or contaminants.

3.2.2 Scanning electron microscopy (SEM) studies

Since the multiferroic properties including dielectric, impedance, ferroelectric and magnetoelectric coupling coefficient depend strongly on their microstructures, scanning electron microscopy (SEM) was used at room temperature to examine the sintered pellets of BMFO and BCoFMO samples for their microstructural characteristics. Figure 4 displays the resulting SEM micrographs (a, c). Images reveal that the microstructures are comprised of submicron-sized clusters contained within several grains. BMFO sample grain growth appears to be predominantly continuous, but BCoFMO sample grain growth appears to be discontinuous in certain places.

The measured microstructures of both samples reveal that the BMFO sample exhibits superior grain development in comparison to BCoFMO. Due to the low melting point of Bi in this sample, the comparatively low sintered temperature (700 °C/4 h) may not be adequate to process liquid phase-assisted grain formation. In addition, SEM pictures of both samples with Mn doping reveal that the particles in certain places, where the high melting point Mn is likely to be abundant, have not yet participated in the grain growth process, resulting in shades of discontinuous grain growth. However, it appears from the photos that the microstructures of both samples are transforming into uniformly scattered spherical grains with almost no intragranular porosity. It means that the vast majority of the porosity observed in the pictures, regardless of its size, originates from intergranular pores. Using imageJ software [12], the grain sizes of the two multiferroic BFMO and BCoFMO samples were determined to be 1.24 μm for BFMO and 0.98 μm for BCoFMO samples, respectively.

Figure 4 depicts the energy dispersive X-ray spectra (EDAX) that were obtained to determine the chemical equilibrium of the sintered samples (b, d). The patterns quantify the presence of every element present in both samples. In addition, these spectra demonstrate that neither of the samples contains any additional elements. The EDAX analysis of the patterns enables estimation of the elemental concentrations quantitatively present in the samples, and the obtained weight% values of the BFMO sample are 61.65%, 17.90%, 0.46 and 19.99% for bismuth, iron, manganese and oxygen, respectively; and the weight% values of the BCoFMO sample are 45.31%, 2.56%, 32.42%, 0.14%, and 19.57% for bismuth, cobalt, manganese, iron, Taking into account the molecular weights of all the elements, the respective mole percentages of the concentrations in each sample were estimated, and the obtained ratio of elements is close to the empirical formula of the BFMO system (64.80%,

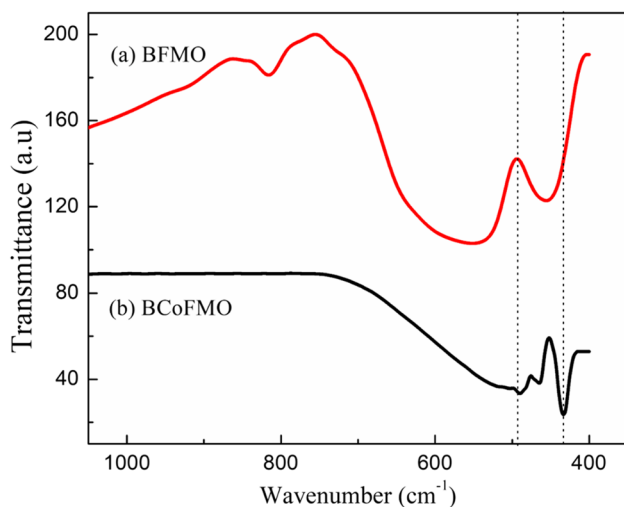


Fig. 2 FTIR patterns of **a** BFMO and **b** BCoFMO multiferroic samples

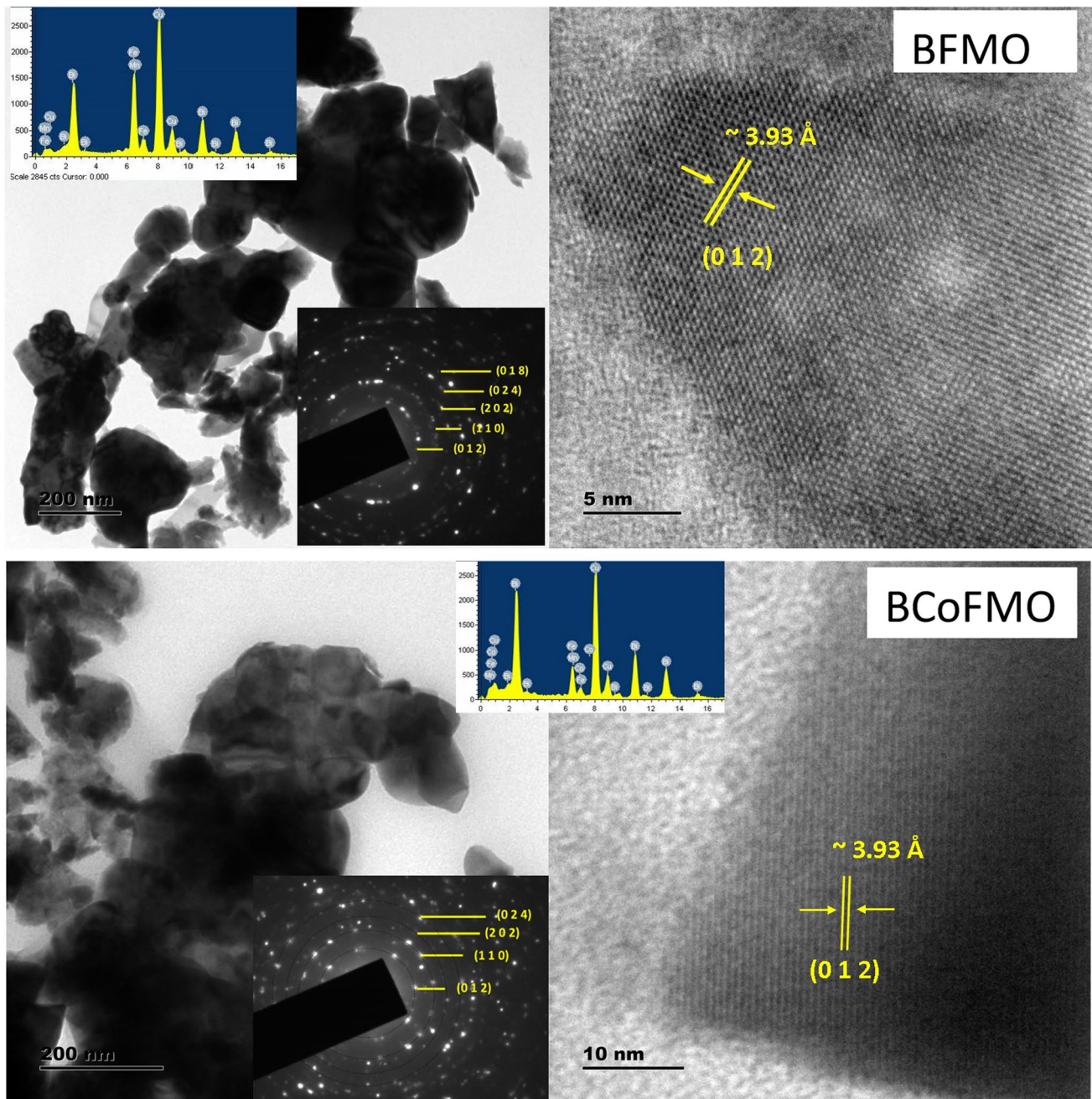


Fig. 3 HRTEM micrographs along with the corresponding SAD patterns of BFMO and BCoFMO multiferroic samples

17.64%, 0.43%, and 16.13% for bismuth iron and oxygen, respectively), confirming that the obtained materials were identical to those of the intended samples.

3.3 Magnetic measurements (M–H loops)

Figure 5, shows the magnetization (M) vs magnetic field (H) hysteresis loops for both the BFMO and BCoFMO samples at room temperature. The magnitude of the magnetic moments created in the multiferroic samples and

the undoped BFO was estimated by plotting graphs of the magnetization values in their respective weights against the applied magnetic field. M – H loops, as seen in Fig. 5, are present when magnetic order is present, as expected. In contrast to BCoFMO (cobalt and manganese co-doped BFO), the BMFO sample (only Mn doped BFO sample) exhibits weak magnetic order with the traces of typical antiferromagnetic character, as seen in M – H loop observations. High levels of coercivity and retentivity may be seen in the BCoFMO sample, as depicted in the inset figure. Maximum magnetization

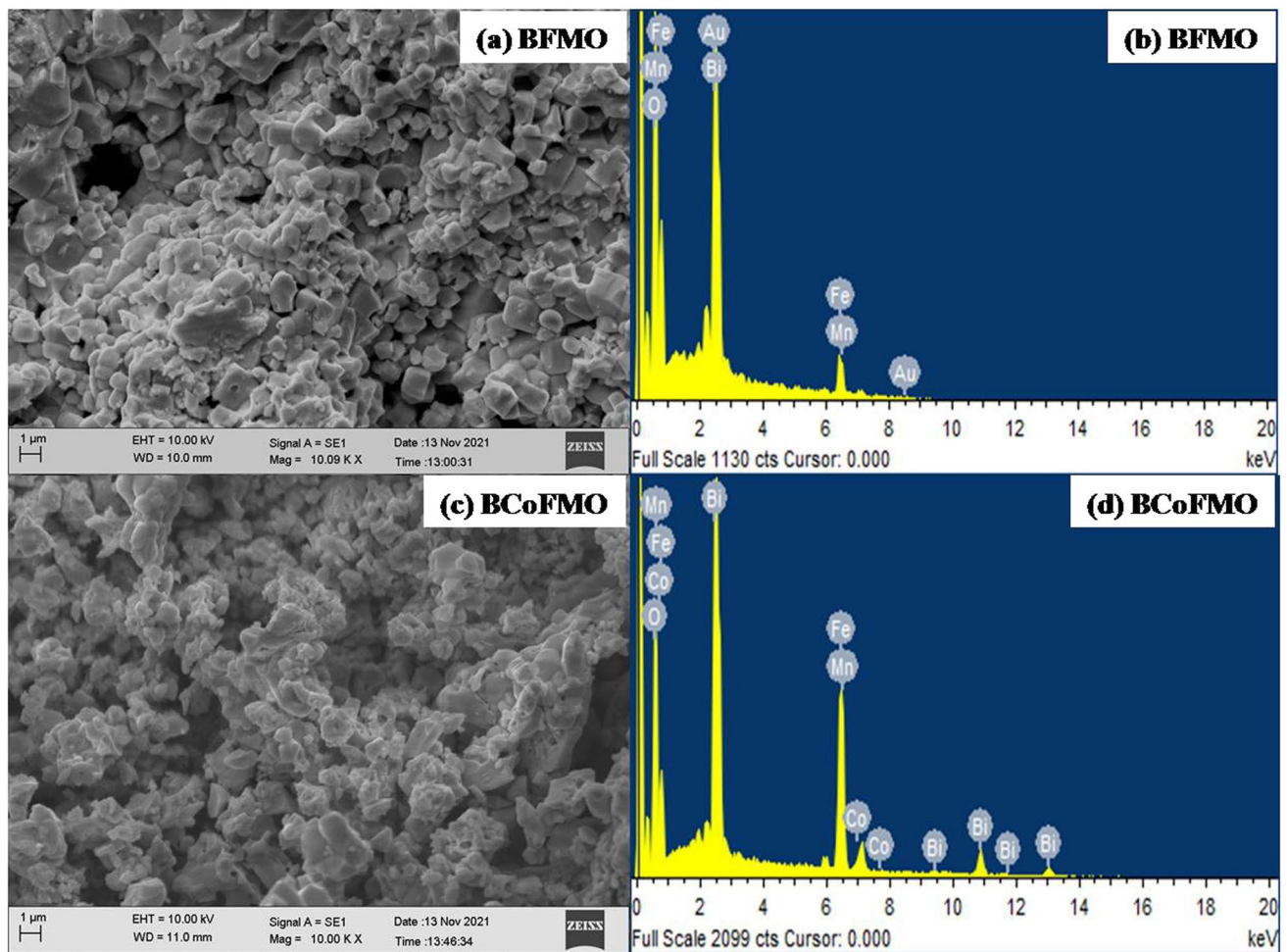


Fig. 4 a, c SEM micrographs and b, d EDAX spectra of BFMO and BCoFMO multiferroic samples

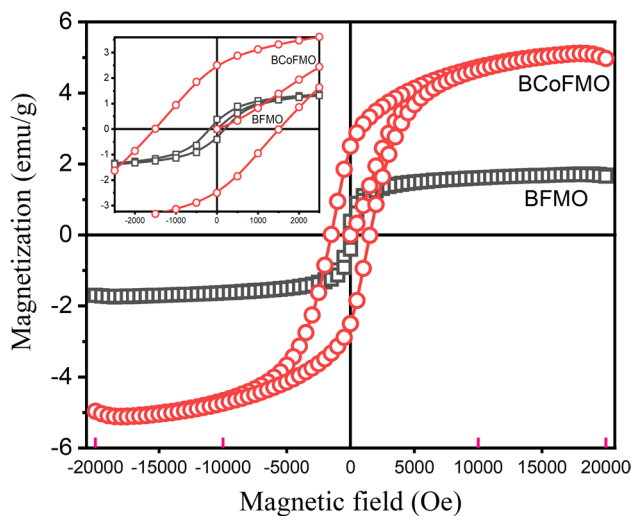


Fig. 5 Room temperature M–H loops of BFMO and BCoFMO samples

values of 1.7345 emu/g and 5.1204 emu/g were measured for BFMO and BCoFMO, respectively. It is well established that the presence of G-type anti-ferromagnetism in an uncompensated cycloidal spin structure in a bismuth ferrite sample always acts to stifle the formation of a magnetic order and, ultimately, a magnetization. To get around this problem, present work aimed to chosen to alter the cycloid spin structure of BFO by inserting magnetically active manganese (Mn) ions and transition metal ions of cobalt into the crystal lattice. The observed results suggest that these alterations would modify the crystal structure of BFO to correct the cycloidal symmetry, leading to increased magnetic order in both samples. Here, the effect of co-doping raised owing to both Mn and Co in the lattice of bismuth ferrite can be attributed to the increased magnitudes for magnetization, coercivity, and retentivity in the BCoFMO sample [22–26]. The table lists all the values explicitly. Smaller particle sizes (40–46 nm) were detected in the current investigation, which is credited with improving magnetic order and other magnetic characteristics in both samples. Although the BFMO

sample has smaller particles than the BCoFMO sample, it may have higher magnetic order due to contributions generated by cobalt ions and manganese ions from separate lattice locations and their respective cationic distributions. However, in other samples, the migration of ions (responsible for cationic distribution) may also involve $\text{Co}^{2+}/\text{Co}^{3+}$ and $\text{Mn}^{2+}/\text{Mn}^{3+}$, however in the BFMO sample, the consequent movement of ions is solely relying on these ions (Bohr magnetons). Because of this, BCoFMO has the potential to produce a larger amount of Bohr magnetons in the sample than BFMO. Since the availability of magnetic cations and their effect in terms of existing Bohr magnetons determines the strength of the magnetic exchange interactions in any magnetic system. Therefore, the current system of doped samples will benefit from the influence of transition metal ions along with Mn to increase the number of cations and Bohr magnetons, leading to an improvement in the magnetic order in BCoFMO. In addition, the structural changes in the bismuth ferrite lattice are successfully influenced by these alterations, leading to the suppression of the cycloid spin structure with appropriate and equal anisotropic compensations, as shown by the coercivities of + 186.65 Oe and – 188.23 Oe in the BFMO sample and + 1499.05 Oe and – 1501.13 Oe in the BCoFMO sample.

3.4 Dielectric studies

3.4.1 Frequency dependent dielectric constant

The electric properties of a multiferroic material, it is common knowledge, are affected by the concentration of free charge carriers and the direction in which the material is oriented relative to an external electric field. Polarization (dielectric constant) is a function of frequency and temperature that is produced by the motion of charge carriers in response to an external electric field. Before anything else, observation on how the ions reacted to an applied electric field by taking dielectric measurements at different frequencies was done. Hopping processes (if any) may be proposed as a possible explanation for the conduction phenomenon seen in these samples. Dielectric constant and loss tangent for room temperature (RT) tests of BFMO and BCoFMO samples from 1 Hz to 10 MHz are shown in Fig. 6. It is clear from the patterns that there are significant variances in the dielectric constant values between the samples, particularly at the lower frequencies (up to 10 Hz). Aside from a very narrow band of frequencies, both samples show remarkably similar tendencies across the board. The frequency response of $\tan \delta$ for the two samples is shown in the inset of Fig. 6. This trend exhibits typical dielectric loss behaviour, with distinct dielectric loss peak frequencies [27].

What follows is a description of the typical dielectric behaviour of both samples. The purity of the sample, the

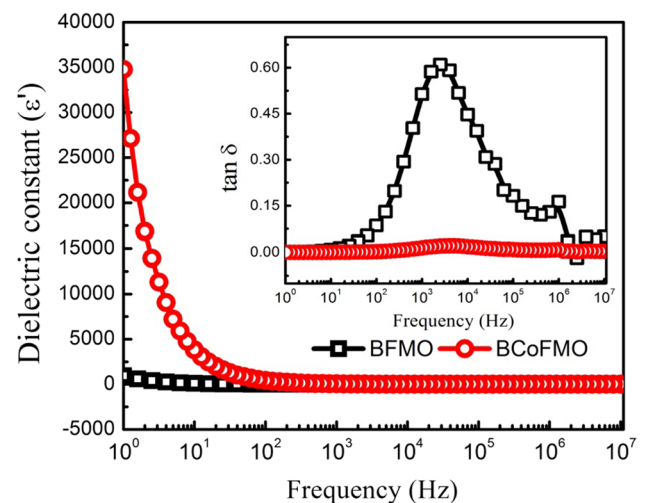


Fig. 6 Frequency response of dielectric constant and $\tan \delta$ (inset) for BFMO and BCoFMO multiferroic samples at RT

presence of free charge carriers, and the efficiency of the locking mechanisms all contribute to a higher dielectric constant in ferrite and multiferroic systems, respectively. However, in many systems made up of various vacancies (oxygen) and microscopic defects, it is possible to get a higher dielectric constant [11]. In contrast, the multivalent (divalent, trivalent, and tetravalent) ions present in these samples and their corresponding hopping mechanisms may be responsible for the dielectric behaviour in this system of samples. A controlled dielectric phenomenon with sufficient dielectric dispersion and nearly comparable trends was presented as the efficient locking mechanism in both samples. Multiple reports [11] indicated that the dielectric constant decreased when Mn was included in the mixture. The free charges can be effectively locked in place through the use of hopping processes, such as $\text{Mn}^{3+} + \text{Fe}^{3+} \rightleftharpoons \text{Fe}^{2+} + \text{Mn}^{4+}$, $\text{Mn}^{3+} \rightleftharpoons \text{Mn}^{2+}$ and $\text{Fe}^{3+} \rightleftharpoons \text{Fe}^{2+}$ for the BFMO and, $\text{Co}^{3+} + \text{Fe}^{3+} \rightleftharpoons \text{Fe}^{2+} + \text{Co}^{4+}$, $\text{Mn}^{3+} + \text{Fe}^{3+} \rightleftharpoons \text{Fe}^{2+} + \text{Mn}^{4+}$, $\text{Fe}^{3+} \rightleftharpoons \text{Fe}^{2+}$, $\text{Mn}^{3+} \rightleftharpoons \text{Mn}^{2+}$ and $\text{Co}^{3+} \rightleftharpoons \text{Co}^{2+}$. For this reason, the inclusion of extra charge carriers, like Mn and Mn/Co with their multivalent states, can effectively work on the locking mechanism and, in turn, reduce strain in these samples. Electron hopping between identical ions existing in different valence states can increase polarisation, whereas locking through charge-balanced couples between different ions existing in different valence states might reduce polarization. Furthermore, to the obstacles caused by the microstructural characteristics of pores, impurities, grains, and grain boundaries, the resistivity of the material impedes the flow of charge carriers and contributes to the reduction of polarisation [27]. Figure 6's inset shows that the BCoFMO sample, in comparison to the other sample, has a higher dielectric constant value and lower dielectric losses.

This is most likely attributable to the co-doping of Co and Mn, which results in a locking mechanism and a corresponding decrease in oxygen vacancies. Since the entire study was conducted at frequencies between 1 Hz and 10 MHz [28–33], all analysed samples also show dipolar polarisation at lower frequencies and space charge polarisation at higher frequencies.

3.4.2 Temperature dependent dielectric constant

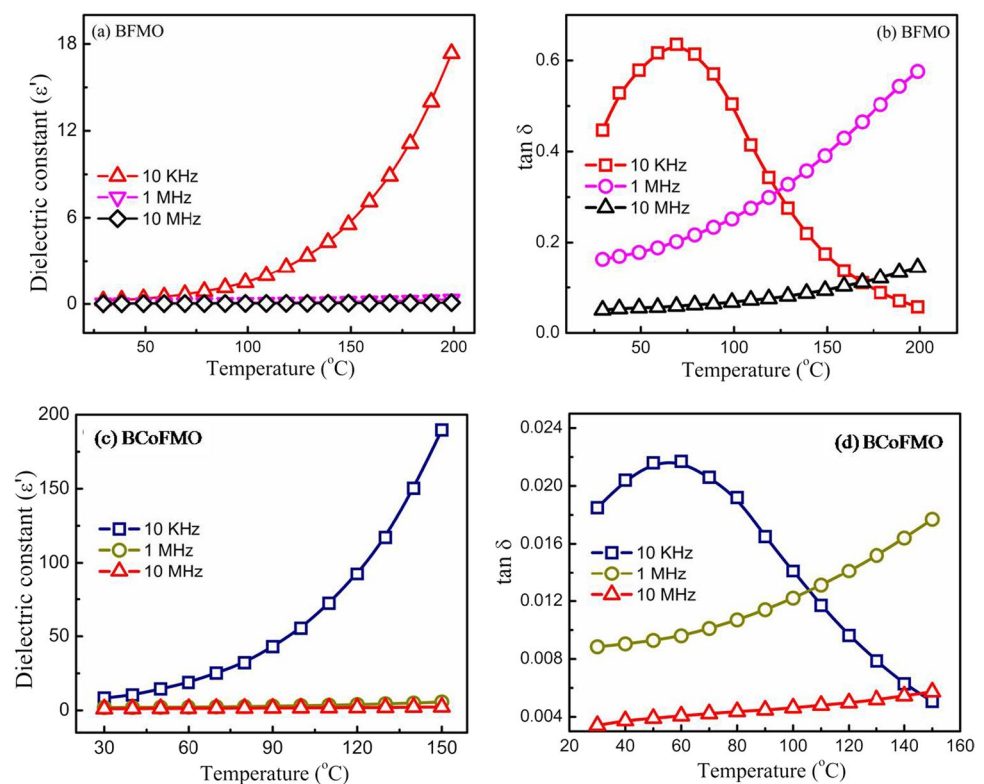
As can be seen in Fig. 7a, c, both BFMO and BCoFMO samples were subjected to temperature-dependent dielectric constant and loss tangent ($\tan\delta$) investigations at various frequencies. Figure 7b, d displays the trends of dielectric constant and loss tangent values for BFMO and BCoFMO samples under temperature treatment at different frequencies, with very small magnitudes for loss tangent. On the other hand, constant variation in the dielectric constant with the application of temperature was evident in both the samples at all frequencies. Higher magnitudes of dielectric constant have been reported at lower frequencies, while lower magnitudes have been observed at higher frequencies, suggesting the occurrence of typical space charge polarisation in both samples [28]. Compared to the BFMO sample, the BCoFMO sample displays much larger magnitudes for dielectric constant and much smaller magnitudes for dielectric loss tangent (which is analogous to the frequency variation). Further evidence indicates the multivalent ions in the

BCoFMO sample have an efficient locking mechanism that will operate to boost the polarisation phenomena and, in turn, the effective dielectric parameters. Both samples are promising for device use because of their high dielectric constant and low dielectric loss.

3.5 Impedance studies

Complex impedance spectroscopy studies, which involve the real (Z') and imaginary (Z'') components with respect to frequency and temperature, are an efficient method for deducing the relation between the structural parameters (grain and grain boundary) and the relevant electric properties of the materials. These graphs prove the roles played by grain and grain boundary interfaces, and by extension, the potential hopping mechanisms in this system. The conduction mechanism driven by grains and grain boundaries can then be inferred from the relationship between the Z' and Z'' (Nyquist plots) [34]. These diagrams include a single semicircle, two semicircles, or even three semicircles, depending on the system and the dominant hopping processes and the contributions they produce. The roles played by grain borders and grains are revealed by research at lower and higher frequencies. Interface or electrode effects may be responsible for the third semicircle (if present) at higher frequencies [35]. Real impedance (Z') at RT for both BFMO and BCoFMO samples is shown in Fig. 8a as a function of frequency. The measured trends make it clear that, like the

Fig. 7 a, c Temperature dependence of dielectric constant (ϵ') and b, d $\tan\delta$ for BFMO and BCoFMO multiferroic samples at different frequencies



behaviour of dielectric dispersion, the actual impedance is larger at lower frequencies and smaller at higher frequencies. As a result of space charge effects in both multiferroic systems, dispersion is seen for both samples at 10 kHz, and both trends have been observed to merge. Similar to the discussion in the dielectric dispersion with frequency [36], the hopping mechanisms originating from distinct multivalent ions may cause a smaller variance in the magnitudes of actual impedance for both samples. The Z' frequency response for the two samples is displayed in Fig. 8b. The dispersion frequency reported in the real impedance analysis is consistent with the single broad peak seen in the curves at low frequency (10 kHz) for both samples.

The relaxation qualities of these two samples are reflected in the fact that the peaks occur at distinct frequencies. In general, the loss spectrum has peaks in the steady state where the hopping frequency of the localised electrons is almost equal to the frequency of the applied field. Moreover, the existing free charge carriers' ability to align with the field and/or immobile species in the respective systems is the source of these peaks.

Graphs of the complex impedance (Z' vs Z'') at room temperature are shown in Fig. 9. Figure shows that the two samples have several similarities, including a single semicircular arc followed by an origin with a second semicircular arc. This may suggest that the samples' conduction mechanisms have different origins, but it might also just be a coincidence. Considering that the distributions obtained from grain boundary contributions may be the most prominent one in this case for both sets of samples, low-frequency trends are of particular interest. The system's grain property, shown by the semicircle in the high-frequency region, is the result of the parallel combination of the grain's resistance (R_g) and capacitance (C_g). The semicircle in the low-frequency region is also attributed to the grain boundary features that

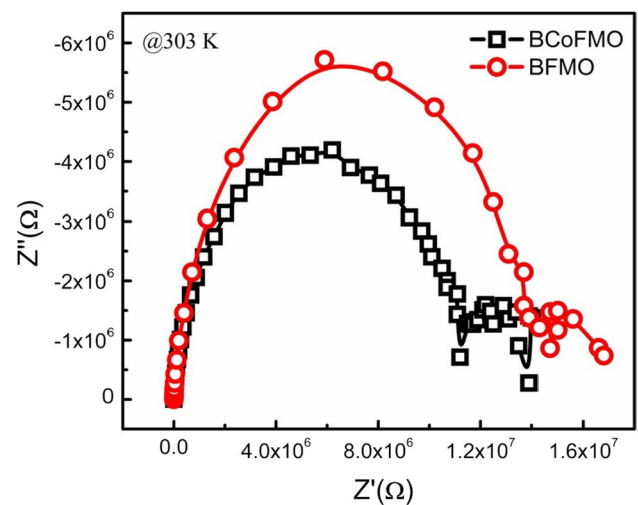


Fig. 9 Nyquist plots (Z' versus Z'') for BFMO and BCoFMO multiferroic samples at RT

stem from the parallel combination of the grain boundary resistance (R_{gb}) and grain boundary capacitance (C_{gb}) of the system. Importantly, semicircular behaviours have been seen for these samples, which is suggestive of Debye-type relaxation [37–41].

4 Conclusions

Wet chemical synthesis of sol–gel autocombustion technique has produced nanoscale manganese doped bismuth ferrite (BFMO) and Co/Mn co-doped BFMO (BCoFMO) multiferroic samples. XRD shows all samples have single-phase perovskite structures with rhombohedral symmetry. HRTEM tests show typical particle sizes of 40–46 nm. XRD

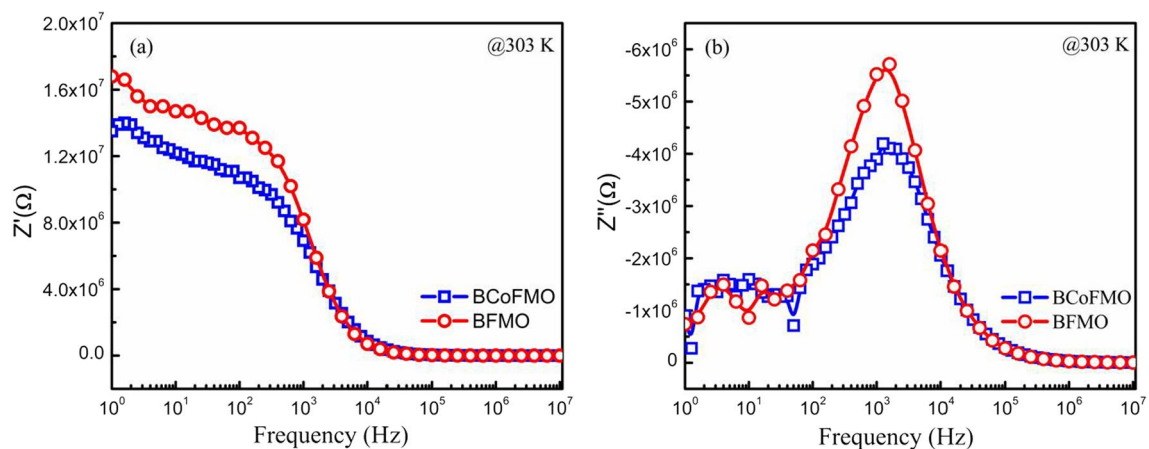


Fig. 8 **a** Frequency response of real component of impedance. **b** Frequency response of imaginary component of impedance for BFMO and BCoFMO multiferroic samples at RT

and HRTEM particle sizes matched. SEM micrographs show no intragranular pores. Energy dispersive X-ray spectrum analysis proves the samples are pure and impurity-free. Dielectric and impedance measurements show space charge polarisation and Debye-type relaxation features in both samples with effective locking mechanisms and reduced dielectric losses. Co-doping increases magnetic order in BCoFMO samples compared to BFMO samples. Doping bismuth ferrite may modify its cycloid spin structure and increase magnetic order. These samples are suited for spintronic device applications due to their structural, microstructural, dielectric, impedance, and magnetic enhancements.

Declarations

Conflict of interest On behalf of all authors, the corresponding author states that there is no conflict of interest.

References

- W. Eerenstein, N.D. Mathur, J.F. Scott, *Nature* **442**, 759 (2006)
- J. Wang, J.B. Neaton, H. Zheng, V. Nagarajan, S.B. Ogale, B. Liu et al., *Science* **299**, 1719 (2003)
- D. Khomskii, *Physics* **2**, 20 (2009)
- G. Catalan, J.F. Scott, *Adv. Mater.* **21**, 2463 (2009)
- C.-W. Nan, *Appl. Phys.* **103**, 03110 (2008J)
- M. Marzouk, H.M. Hashem, S. Soltan, A.A. Ramadan, *J. Mater. Sci. Mater. Electron.* **31**, 5599 (2020)
- A. Roy, R. Gupta, A. Garg, *Adv. Condens. Matter Phys.* **2012**, 1–12 (2012)
- S. Ramesh, B. Dhanalakshmi, B.C. Sekhar, P.S.V. Rao, B.P. Rao, C.G. Kim, *J. Nanosci. Nanotechnol.* **16**(10), 11094 (2016)
- K.V. Vivekananda, B. Dhanalakshmi, B.P. Rao, P.S.V.S. Rao, *Appl. Phys. A* **127**(3), 1 (2021)
- Y.-J. Zhang, H.-G. Zhang, J.-H. Yin, H.-W. Zhang, J.-L. Chen, W.-Q. Wang et al., *J. Magn. Magn. Mater.* **322**, 2251 (2010)
- B. Dhanalakshmi, B.C. Sekhar, K.V. Vivekananda, B.S. Rao, B.P. Rao, P.S.V. Subba Rao, *Appl. Phys. A* **126**(7), 1 (2020)
- H.W. Chang, F.T. Yuan, K.T. Tu, S.Y. Lin, C.R. Wang, C.S. Tu, *J. Alloys. Compd.* **683**, 427 (2016)
- V.P. Reddy, R.V. Mangalaraja, N.V. Giridharan, M. Ashok, *J. Alloys. Compd.* **684**, 55 (2016)
- M. Salavati-Niasari, F. Davar, M. Farhadi, *Sol Gel Sci. Technol.* **51**, 48 (2009J)
- K.C. Patil, *Bull. Mater. Sci.* **16**, 533 (1993)
- S. Ckkraborty, S. Mukherjee, S. Mukherjee, *J. Aust. Ceram. Soc.* **51**(1), 45–53 (2015)
- K. Sreekanth, B. Dhanalakshmi, D. Madhavaprasad, *J. Ind. Chem. Soc.* **99**(9), 100649 (2022)
- B. Dhanalakshmi, K. Pratap, B.P. Rao, P.S.V.S. Rao, *J. Alloys. Compd.* **676**, 193 (2016)
- A.T. Raghavender, N.H. Hong, *J. Mag.* **16**, 19 (2011)
- R.D. Shannon, *Acta Cryst. A* **32**, 751 (1976)
- <http://imageJ.nih.gov>
- R. Das, G.G. Khan, S. Varma, G.D. Mukherjee, K. Mandal, *J. Phys. Chem. C* **117**(39), 2020 (2013)
- M.R. Kanth, B. Dhanalakshmi, P.S.V. Subba Rao, B.P. Rao, *J. Mater. Eng. Perform* **1** (2022)
- M.M. Rhaman, M.A. Matin, M.N. Hossain, M.N.I. Khan, M.A. Hakim, M.F. Islam, *J. Phys. Chem. Solid* **147**, 109607 (2020)
- G.M. Sravani, N. Murali, B.C. Sekhar, B. Dhanalakshmi, D. Parajuli, T.G. Naidu et al., *J. Ind. Chem. Soc.* **99**(6), 100465 (2022)
- C. Beatrice, S. Dobák, V. Tsakaloudi, C. Ragusa, F. Fiorillo, L. Martino et al., *AIP Adv.* **8**, 047803 (2018)
- B. Dhanalakshmi, K. Pratap, B. ParvatheeswaraRao, P.S.V. SubbaRao, *J. Mag. Mater.* **404**, 119 (2016)
- B. Dhanalakshmi, P. Kollu, C.H.W. Barnes, B.P. Rao, P.S.V.S. Rao, *Appl. Phys. A* **124**, 1–8 (2018)
- B. Dhanalakshmi, P.S.V.S. Rao, B.P. Rao, C.G. Kim, *J. Nanosci. Nanotechnol.* **16**, 11089 (2016)
- K. Sarkar, S. Mukherjee, S. Mukherjee, *Process. Appl. Ceram.* **9**(1), 53–60 (2015)
- B. Dhanalakshmi, B. Pratap Kollu, B. Chandra Sekhar, P. Rao, P.S.V. Subba Rao, *Ceram. Int.* **43**, 9272 (2017)
- R. Chakraborty, S. Mukherjee, S. Mukherjee, *J. Aust. Ceram. Soc.* **53**, 57–65 (2017)
- S. Mukherjee, K. Sarkar, S. Mukherjee, *Interceram* **64**(1–2), 38–43 (2015)
- B. Dhanalakshmi, P. Kollu, B.P. Rao, P.S.V.S. Rao, *Ceram. Int.* **42**(2), 2186 (2016)
- J.R. Macdonald, *Chemistry* **223**, 25 (1987)
- M.J. Verkerk, B.J. Middelhuus, A.J. Burggraaf, *Solid State Ion.* **6**, 159 (1982)
- S. Pattanayak, R.N.P. Choudhary, P.R. Das, S.R. Shannigrahi, *Ceram Int.* **40**, 7983 (2014)
- B. Dhanalakshmi, K.V. Vivekananda, B.P. Rao, P.S.V.S. Rao, *Phys. B* **571**, 5 (2019)
- K. Sreekanth, B. Dhanalakshmi, D. Madhavaprasad, *J. Ind. Chem. Soc.* **99**(7), 100565 (2022)
- B.C. Sekhar, B. Dhanalakshmi, B.S. Rao, S. Ramesh, K.V. Prasad, P.S. Rao et al., *Multifunct. Ferroelectr. Mater.* **71**, 1–19 (2021)
- B. Dhanalakshmi, B.C. Sekhar, K.V. Vivekananda, B.S. Rao, B.P. Rao, *Appl. Phys. A* **126**, 1–9 (2020)

Publisher's Note Springer Nature remains neutral with regard to jurisdictional claims in published maps and institutional affiliations.

Springer Nature or its licensor (e.g. a society or other partner) holds exclusive rights to this article under a publishing agreement with the author(s) or other rightsholder(s); author self-archiving of the accepted manuscript version of this article is solely governed by the terms of such publishing agreement and applicable law.